LETTER

doi:10.1038/nature11052

Recurrent network activity drives striatal synaptogenesis

Yevgenia Kozorovitskiy[1]*, Arpiar Saunders[1]*, Caroline A. Johnson[1], Bradford B. Lowell[2] & Bernardo L. Sabatini[1]

Neural activity during development critically shapes postnatal wiring of the mammalian brain. This is best illustrated by the sensory systems, in which the patterned feed-forward excitation provided by sensory organs and experience drives the formation of mature topographic circuits capable of extracting specific features of sensory stimuli[1,2]. In contrast, little is known about the role of early activity in the development of the basal ganglia, a phylogenetically ancient group of nuclei fundamentally important for complex motor action and reward-based learning[3,4]. These nuclei lack direct sensory input and are only loosely topographically organized[5,6], forming interlocking feed-forward and feed-back inhibitory circuits without laminar structure. Here we use transgenic mice and viral gene transfer methods to modulate neurotransmitter release and neuronal activity *in vivo* in the developing striatum. We find that the balance of activity between the two inhibitory and antagonist pathways in the striatum regulates excitatory innervation of the basal ganglia during development. These effects indicate that the propagation of activity through a multi-stage network regulates the wiring of the basal ganglia, revealing an important role of positive feedback in driving network maturation.

Excitatory input from the cortex and thalamus enters the basal ganglia through the striatum, where it is locally processed and transformed into two inhibitory, GABAergic outputs called the direct and indirect pathways[7]. Each pathway arises from a distinct class of spatially intermixed medium spiny neurons (MSNs) with differing projections and molecular characteristics[8]. These projection patterns suggest opponent effects on basal ganglia output: direct pathway MSNs form synapses in substantia nigra reticulata (SNr), the basal ganglia output nucleus, whereas indirect pathway MSNs form synapses in globus pallidus, which in turn inhibits the SNr[9]. Because the SNr provides GABAergic inhibition to the thalamus, which subsequently activates cortex through glutamatergic synapses, the interactions of basal ganglia, thalamus and cortex can be simplified as a closed loop, differentially controlled by the direct and indirect pathways (Supplementary Fig. 1). Anatomical evidence supports this model[10,11] and the opponent roles of the two pathways on motor behaviour have been recently demonstrated in adult rodents[12,13]. In addition, *in vivo* recordings and circuit tracing indicate that different corticostriatal inputs are processed through segregated, parallel networks[6,10,11,14]. Given this organization, establishing correct wiring of the cortex-basal ganglia–thalamus circuitry poses a significant developmental challenge, requiring that functional interactions be maintained over polysynaptic networks comprised of mixed inhibitory and excitatory projections.

To investigate how striatal activity contributes to circuit development, we generated mice incapable of releasing GABA from direct or indirect pathway MSNs through conditional knockout of *Slc32a1*, which encodes the vesicular GABA transporter (VGAT) (Fig. 1)[15]. GABAergic neurons lacking VGAT are unable to package GABA into synaptic vesicles for release[16,17]. Pathway specificity was conferred by bacterial artificial chromosome (BAC) transgenic mice that express Cre recombinase under the control of the type 1a or type 2 dopamine receptors[18]. In *Drd1a* Cre (D1-Cre) mice, Cre expression in GABAergic neurons is largely limited to direct pathway MSNs, although Cre is also found in non-GABAergic cortical neurons (Fig. 1a and Supplementary Figs 2 and 3). In *Drd2* Cre (D2-Cre) mice, Cre expression is largely limited to indirect pathway MSNs (Fig. 1a and Supplementary Fig. 2). Mice with *Slc32a1* deletion in direct or indirect pathway MSNs showed opposing locomotor phenotypes and survived

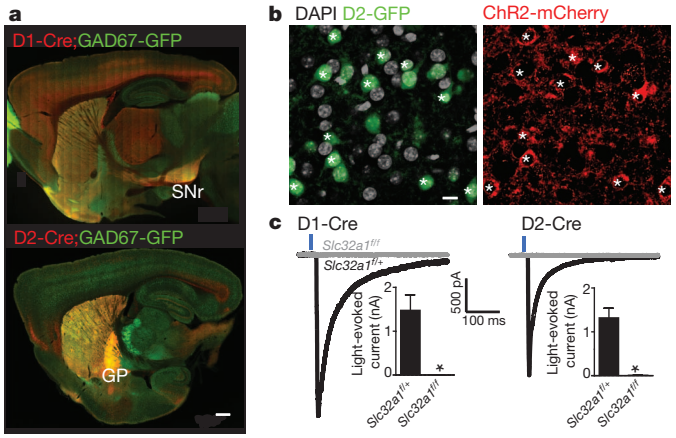

Figure 1 | Conditional knockout of *Slc32a1* from direct or indirect pathway MSNs abolishes GABAergic output. **a**, Cre expression driven by *Drd1a* (D1-Cre, top) and *Drd2* (D2-Cre, bottom) BACs was visualized via activation of tdTomato in a reporter mouse. Red fluorescence reveals expression throughout striatum and in axons in expected target nuclei of direct and indirect pathway MSNs (SNr and globus pallidus (GP), respectively). Green fluorescence reflects expression of a GAD67-GFP transgene that reports GABAergic neurons. As seen in the red channel, there is diffuse cortical expression of Cre in the D1-Cre mice; however, this occurs in non-GABAergic neurons as noted by the lack of overlap with GFP fluorescence (see Supplementary Fig. 2 for complete analysis). Scale bar: 500 μm. **b**, AAV DIO–ChR2–mCherry injected into the striatum of a mouse carrying D2-Cre and D2-GFP transgenes shows ChR2–mCherry labelling in GFP^+ cells, indicating pathway-specific conditional expression of the virally encoded protein. ChR2–mCherry-expressing somata are marked with an asterisk and represent over two-thirds of the GFP^+ MSNs in the area of dense infection. ChR2–mCherry was never observed in GFP^- MSNs in these mice. Scale bar: 10 μm. **c**, Voltage-clamp recordings from ChR2–$mCherry^-$ MSNs demonstrate GABAergic synaptic currents evoked by 2-ms-long pulses of 473-nm light that stimulates neighbouring ChR2–$mCherry^+$ MSNs. Example currents from MSNs in D1-Cre (left) and D2-Cre (right) mice that were either homozygous (grey, $Slc32a1^{f/f}$) or heterozygous (black, $Slc32a1^{f/+}$) for the *Slc32a1* conditional allele are shown. GABAergic currents are inward due to high intracellular Cl^- concentration. Insets: graphs of average peak current amplitudes evoked in mice of each genotype. $*P < 0.05$ for comparison of $Slc32a1^{f/+}$ and $Slc32a1^{f/f}$ data. Error bars indicate s.e.m.

[1]Howard Hughes Medical Institute, Department of Neurobiology, Harvard Medical School, 220 Longwood Ave, Boston, Massachusetts 02115, USA. [2]Endocrinology Division, Beth Israel Deaconess Medical Center, 330 Brookline Avenue, Boston, Massachusetts 02215, USA.
*These authors contributed equally to this work.

until weaning (Supplementary Fig. 4), a time of increasing reliance on reward-based complex motor actions.

To test the efficacy of silencing of GABA release we relied on optogenetic analysis of MSN-to-MSN collateral synapses[19]. Channelrhodopsin 2–mCherry fusion protein (ChR2–mCherry) was expressed in Cre-positive MSNs by injecting an adeno-associated virus (AAV) containing a double floxed inverted ChR2–mCherry transgene into the striatum at postnatal (P) days 3–5 (Fig. 1b)[20]. Whole-cell voltage-clamp recordings of ChR2-negative MSNs demonstrated light-evoked GABAergic currents in acute brain slices from P13–18 *D1-cre;Slc32a1*$^{f/+}$ mice ($-1{,}477 \pm 352$ pA, $n = 20$) and *D2-cre;Slc32a1*$^{f/+}$ mice ($-1{,}319 \pm 221$ pA, $n = 12$); these currents were absent in littermate *Slc32a1*$^{f/f}$ mice (*D1-cre;Slc32a1*$^{f/f}$, -2.19 ± 1.6 pA, $n = 7$; *D2-cre;Slc32a1*$^{f/f}$, -9.91 ± 2.4 pA, $n = 7$) (Fig. 1c and Supplementary Fig. 5).

We examined whether GABA release from MSNs is required for cell survival and long-range axonal projections. The proportion of Cre^{+} cell nuclei was 45–48% in D1-Cre and D2-Cre mice and independent of the number of conditional *Slc32a1* alleles (Supplementary Fig. 6). MSNs lacking GABA release form qualitatively normal long-range axonal projections, on the basis of examination of ChR2–mCherry fluorescence in the SNr and globus pallidus (SNr, 18–19%; globus pallidus, 15–16% fractional area coverage) (Supplementary Fig. 7). These observations confirm that MSNs lacking GABA release are maintained in normal numbers and extend grossly normal axons.

In contrast, silencing GABA release had profound consequences on the number of excitatory synapses received, which are typically associated with dendritic spines[21,22]. In the rodent striatum, inhibitory synapse density is relatively constant throughout postnatal development, whereas excitatory synapse density rises markedly between P10 and P21 (ref. 23). Therefore, we restricted analyses to pairs of littermate control and *Slc32a1* null mice at P14–15. We identified MSNs of each pathway using ChR2–mCherry expression delivered by either Cre-On or Cre-Off AAVs (Supplementary Fig. 8a) (A. Saunders, C. Johnson and B. Sabatini, manuscript in preparation). Even within this narrow developmental window, we detected an increase in miniature excitatory postsynaptic current (mEPSC) frequencies, but not amplitudes, among littermates of the same genotype (frequency: P14, 0.14 ± 0.06 Hz; P15, 0.34 ± 0.1 Hz; amplitude: P14, 14.4 ± 1.0 pA; P15, 13.9 ± 0.4 pA) (Supplementary Fig. 8b). In mice lacking GABA release in direct pathway MSNs, mEPSC frequency was reduced in both direct and indirect pathway MSNs compared to heterozygous sibling controls (direct pathway MSNs: *D1-cre;Slc32a1*$^{f/+}$, 0.22 ± 0.04 Hz, $n = 18$; *D1-cre;Slc32a1*$^{f/f}$, 0.08 ± 0.02 Hz, $n = 16$; indirect pathway MSNs: *D1-cre;Slc32a1*$^{f/+}$, 0.32 ± 0.07 Hz, $n = 14$; *D1-cre;Slc32a1*$^{f/f}$, 0.1 ± 0.03 Hz, $n = 15$) (Fig. 2a, c). Conversely, mEPSC frequency was increased in MSNs of mice with output-silenced indirect pathway (direct pathway MSNs: *D2-cre;Slc32a1*$^{f/+}$, 0.11 ± 0.04 Hz, $n = 9$; *D2-cre;Slc32a1*$^{f/f}$, 0.28 ± 0.07 Hz, $n = 6$; indirect pathway MSNs: *D2-cre;Slc32a1*$^{f/+}$, 0.15 ± 0.06 Hz, $n = 5$; *D2-cre;Slc32a1*$^{f/f}$, 0.37 ± 0.04 Hz, $n = 14$) (Fig. 2b, d). mEPSC amplitudes were largely unaffected by either manipulation (Supplementary Fig. 8c, d).

Changes in mEPSC rates were paralleled by alterations in dendritic spine density, indicating concurrent changes in structural and functional correlates of excitatory synapse number. Dendritic spine density of all MSNs was decreased by silencing the direct pathway (direct pathway MSNs: *D1-cre;Slc32a1*$^{f/+}$, 0.84 ± 0.03 spines per μm, $n = 6$; *D1-cre;Slc32a1*$^{f/f}$, 0.45 ± 0.05 spines per μm, $n = 7$; indirect pathway MSNs: *D1-cre;Slc32a1*$^{f/+}$, 0.68 ± 0.05 spines per μm, $n = 5$; *D1-cre;Slc32a1*$^{f/f}$, 0.41 ± 0.02 spines per μm, $n = 5$) and increased by silencing the indirect pathway (direct pathway MSNs: *D2-cre;Slc32a1*$^{f/+}$, 0.41 ± 0.02 spines per μm, $n = 6$; *D2-cre;Slc32a1*$^{f/f}$, 0.63 ± 0.08 spines per μm, $n = 6$; indirect pathway MSNs: *D2-cre;Slc32a1*$^{f/+}$, 0.56 ± 0.03 spines per μm, $n = 5$; *D2-cre;Slc32a1*$^{f/f}$, 1.02 ± 0.05 spines per μm,

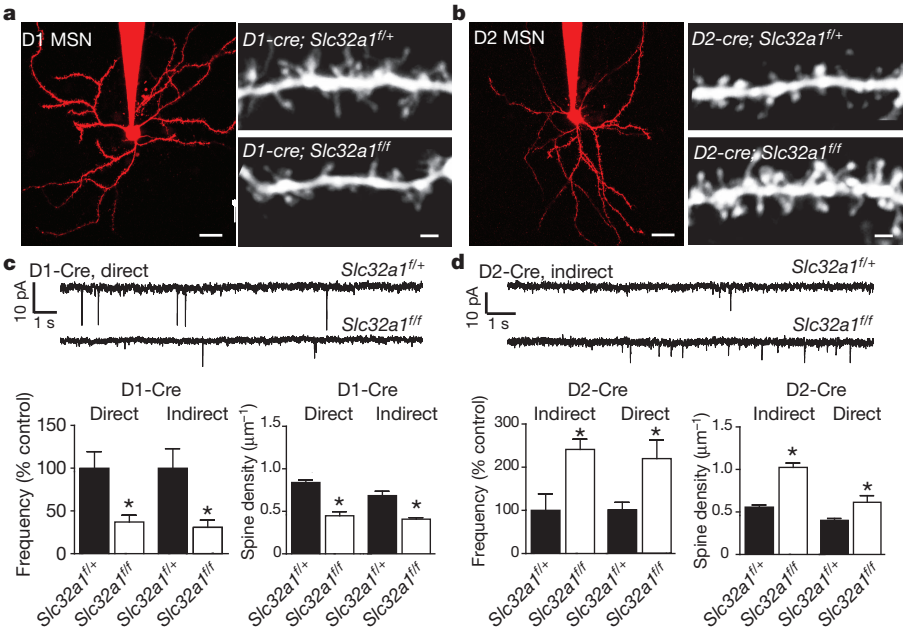

Figure 2 | Conditional knockout of *Slc32a1* in direct and indirect pathway MSNs results in opposing changes to excitatory synapse number. **a**, Left: two-photon laser-scanning microscopy image of a direct pathway *Slc32a1*$^{f/+}$ MSN filled with Alexa Fluor 594 through the recording pipette during whole-cell voltage-clamp analysis of mEPSCs. Right: at a higher magnification, dendritic spines are visible. Examples of a dendrite from a control direct pathway MSN (top) and of a less spiny dendrite from a direct pathway MSN of a *Slc32a1* null sibling (bottom) are shown. Scale bars: 20 μm, 2 μm. **b**, As in **a**, but illustrating the increase in dendritic spine density seen with silencing of indirect pathway MSNs. **c**, Examples and summary of frequencies of mEPSCs in direct pathway *Slc32a1* null mice and their heterozygous sibling controls. Preventing GABA release from direct pathway MSNs reduced mEPSC frequency, compared to direct pathway MSNs in *Slc32a1*$^{f/+}$ sibling controls (top). The summary graph illustrates the decrease in direct and indirect pathway MSNs that were paralleled by differences in the density of dendritic spines. *$P < 0.05$ for comparison of *Slc32a1*$^{f/+}$ and *Slc32a1*$^{f/f}$ data. **d**, As in **c** but for indirect pathway mutants indicating that preventing GABA release from indirect pathway MSNs increased mEPSC frequency and dendritic spine density in indirect and direct pathway MSNs. *$P < 0.05$ for comparison of *Slc32a1*$^{f/+}$ and *Slc32a1*$^{f/f}$ data. Error bars indicate s.e.m.

$n = 6$) (Fig. 2). Together these data show that the degree of excitatory innervation of MSNs is determined by striatal output, such that excitatory hypo- or hyper-innervation is triggered by silencing the direct or indirect pathway, respectively.

Complementary, pathway-dependent effects on excitatory input could be due to cell-intrinsic differences in direct and indirect pathway MSNs. Alternatively, common activity-dependent wiring rules could be differentially activated by each perturbation of basal ganglia output. For example, a net increase in SNr inhibitory output, caused by silencing direct pathway MSNs, could diminish thalamic and cortical activity, decreasing glutamate release and glutamatergic synapse formation in the striatum. In contrast, silencing the indirect pathway could have the converse set of effects (Supplementary Fig. 1b–d). The observation that direct or indirect pathway MSNs show similar perturbations despite selective deletion of *Slc32a1* only in MSNs of the Cre-expressing pathway (Fig. 2) provides support for the circuit-level model.

To test for cell-autonomous, *Slc32a1*-dependent regulation of glutamatergic innervation, we deleted *Slc32a1* in a small and sparse subpopulation of striatal neurons by injecting small quantities of AAV encoding Cre–mCherry into *D2-GFP;Slc32a1*$^{f/f}$ mice at P0–1 (Supplementary Fig. 9a, b). Analysis of mEPSCs and dendritic spines in neighbouring Cre^{+} and Cre^{-} MSNs (identified by nuclear mCherry fluorescence) belonging to the direct and indirect pathway (identified by GFP expression) revealed no changes in mEPSC frequency or dendritic spine density (Supplementary Fig. 9c–e). Thus, *Slc32a1*-dependent, cell-intrinsic mechanisms are unlikely to contribute to differential effects on glutamatergic innervation seen with silenced direct or indirect pathways.

We examined the consequences of manipulating striatal activity specifically during the period of striatal excitatory synaptogenesis[23] using the RASSL (G-protein-coupled receptor activated solely by a synthetic ligand) hM4D[24,25] in direct or indirect pathway MSNs (Fig. 3). hM4D is activated by a blood–brain-barrier-permeable molecule clozapine-*n*-oxide (cno), allowing non-invasive *in vivo* manipulation of neural activity. hM4D couples to the $G\alpha_{i/o}$ pathway, which reduces action potential firing in many cell types (Supplementary Fig. 10) by activating K^{+} channels[13]. AAV carrying the double floxed inverted hM4D–mCherry transgene[25] was injected in D1-Cre or D2-Cre mice at P0–1 and, starting at P8, cno (1 mg kg^{-1}) or saline was administered subcutaneously twice per day to littermate pups. Consistent with our hypothesis, animals with large bilateral injections of AAV to dampen activity of many direct or indirect pathway MSNs, respectively, down- or upregulated mEPSC frequency and dendritic spine density, relative to saline-injected littermates (D1-Cre, direct pathway MSNs: frequency, saline 0.8 ± 0.1 Hz, $n = 18$; cno 0.36 ± 0.07 Hz, $n = 25$; spine density, saline 0.96 ± 0.04 spines per µm, $n = 5$; cno 0.49 ± 0.05 spines per µm, $n = 5$; D2-Cre, indirect pathway MSNs: frequency, saline 0.04 ± 0.01 Hz, $n = 7$; cno, 0.27 ± 0.09 Hz, $n = 8$; spine density, saline 0.54 ± 0.05 spines per µm, $n = 5$; cno 0.98 ± 0.06 spines per µm, $n = 5$) (Fig. 3a–c and Supplementary Fig. 12a). Similar results were observed with the *Adora2a-cre* mouse, based on the adenosine 2A receptor promoter, another Cre driver line for indirect pathway MSNs (Supplementary Fig. 11).

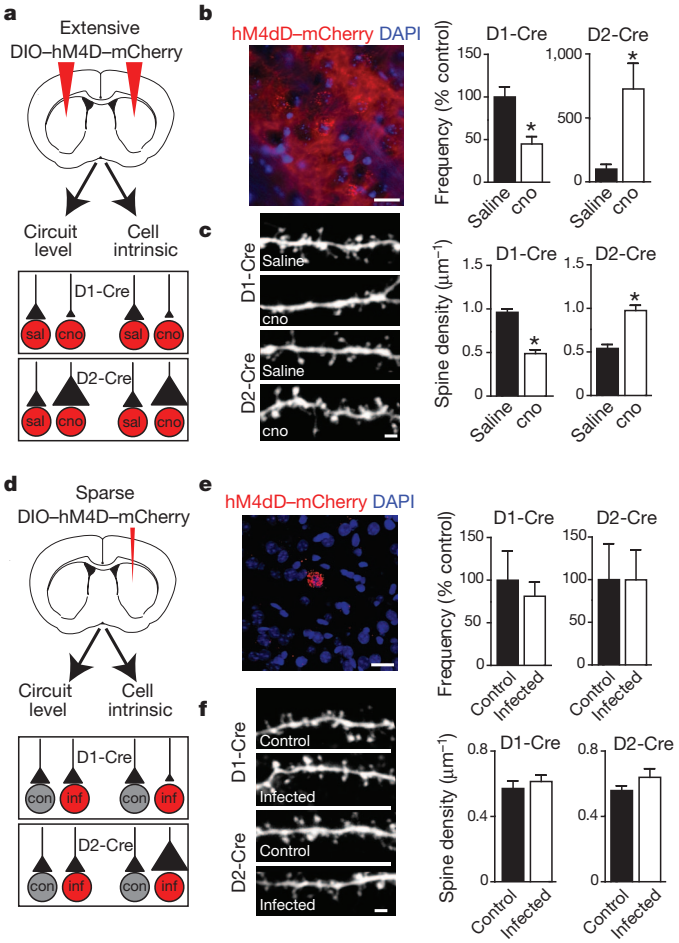

Figure 3 | *In vivo*, developmentally restricted postnatal manipulation of activity in direct and indirect pathway MSNs results in opposing changes to excitatory synapse number. **a**, Schematic of experimental design and hypotheses for changes in excitatory synapse number induced by extensive and bilateral expression of hM4D in direct or indirect pathway MSNs and subsequent injections of cno or saline. Widespread inhibition of direct pathway MSN firing with cno is expected to decrease excitatory synapse number, whether circuit-level or cell-intrinsic mechanisms dictate corticostriatal synaptogenesis. The converse is expected for widespread inhibition of indirect pathway MSNs. **b**, Left: hM4D–mCherry^{+} MSNs in tissue densely infected with hM4D-encoding AAV (mCherry, red; DAPI, blue). Scale bar: 20 µm. Right: summary data demonstrate that *in vivo* manipulation of neuronal activity in direct or indirect pathway MSNs in the time window of excitatory synaptogenesis led to opposing changes in excitatory synapse number. Decreased mEPSC frequency was observed in cno-treated D1-Cre mice, whereas mEPSC frequency was enhanced in cno-treated D2-Cre mice, compared to respective saline-injected controls. *$P < 0.05$ for the comparison of same-pathway MSNs from saline- and cno-injected mice. **c**, Left: top two panels show two-photon laser-scanning microscopy images of a dendrite from a direct pathway MSN in a saline-injected D1-Cre mouse and a less spiny dendrite from a cno-injected sibling. Scale bar: 2 µm. Bottom two images show an example of increased spine density in indirect pathway MSNs of D2-Cre mice treated with cno compared to saline-treated controls. Right: summaries of spine density in cno- and saline-treated mice demonstrating the opposite sign changes resulting from inhibition of the direct or indirect pathway. *$P < 0.05$ for the comparison of same-pathway MSNs from saline- and cno-injected mice. **d**, Schematic of experimental design and hypotheses for possible changes in excitatory synapse number induced by sparse and unilateral expression of hM4D in direct or indirect pathway MSNs and subsequent injections of cno. Manipulation of activity in a small subset of neurons is not expected to engage circuit-wide mechanisms regulating synapse numbers. In contrast, unknown cell-intrinsic mechanisms could regulate the number of synapses formed onto the manipulated neurons, compared to same-pathway uninfected MSNs. **e**, Left: confocal image showing an hM4D–mCherry^{+} MSN in a sparse injection configuration (mCherry, red; DAPI, blue). Scale bar: 20 µm. Right: with sparse activity manipulations, no differences in mEPSC frequency were observed in either direct or indirect pathway infected MSNs, compared to uninfected MSNs. **f**, Left: top two panels show two-photon laser-scanning microscopy images of a dendrite from control or neighbouring hM4D-expressing direct pathway MSN. Bottom two images show spiny dendrites from control or neighbouring hM4D-expressing indirect pathway MSN. Scale bar: 2 µm. Right: summary graph shows that inhibiting activity of a sparse subset of MSNs does not alter dendritic spine density in manipulated direct or indirect pathway neurons. Error bars indicate s.e.m.

In contrast, sparse, unilateral hM4D delivery, designed to have a minimal impact on circuit dynamics, did not alter mEPSC frequency and dendritic spine density in hM4D-expressing neurons relative to uninfected neighbouring MSNs of the same pathway (Fig. 3d–f and Supplementary Fig. 12b). These data also indicate that hM4D-mediated perturbation of G-protein-coupled intracellular signalling pathways is not responsible for the changes in excitatory synapses.

Three lines of evidence—analyses of non-manipulated MSNs in pathway-specific conditional *Slc32a1* knockouts, of sparse *Slc32a1* null MSNs, and of the effects of widespread versus sparse hM4d manipulation of neural activity—support the hypothesis that circuit-level patterns of activity, rather than cell-intrinsic mechanisms, determine the degree of glutamatergic innervation of striatal MSNs. Inherent to this proposed mechanism is the assumption that the basal ganglia output modulates corticostriatal or thalamostriatal glutamatergic activity, which, in turn, regulates excitatory synaptogenesis in the striatum. To probe this mechanism, we directly tested the ability of glutamate exposure to drive spinogenesis in the striatum, and the effect of manipulating corticostriatal activity on striatal spinogenesis and synaptogenesis.

To test whether glutamate release in the striatum is sufficient to induce spinogenesis, we focally stimulated non-spiny segments of P8–11 MSN dendrites with two-photon laser uncaging of glutamate[26,27]. Sparse viral delivery of Cre was used to activate tdTomato reporter fluorescence in a small subset of MSNs in *D2-GFP;Ai14-lsl-tdTomato* mice. Two-photon laser-scanning microscopy was used to monitor dendritic structure during glutamate stimulation (Fig. 4a, b). Stimulation power was calibrated to evoke moderate ~7 pA currents from existing spines (Supplementary Fig. 13). Using protocols that robustly induce synaptogenesis in layer 2/3 pyramidal neurons of developing cortex[26], we observed growth of a new dendritic spine at the glutamate uncaging site in ~50% of trials. The probability of spine growth was similar in direct and indirect pathway MSNs (Fig. 4b), was unaffected by blockade of $GABA_A$ receptors (52% and 50% success percentage for GFP^+ and GFP^- MSNs in control conditions, and 56% and 51%, respectively, in $GABA_A$ antagonist), and matched previous results in cortical pyramidal cells[26]. Thus, glutamatergic stimulation is sufficient to drive spinogenesis in the developing striatum.

To test whether the postnatal activity of corticostriatal projections drives synaptogenesis, we used the *Rbp4-cre* mouse line to express hM4D in corticostriatal neurons emanating from deep cortical layers (Fig. 4c). *Rbp4-cre;D2-GFP* mice were injected with the double floxed inverted AAV carrying hM4D–mCherry at P0–1 and, starting at P8, cno (1 mg kg^{-1}) or saline was administered subcutaneously twice per day to littermate pups. For MSNs of both pathways assayed at P14–15, mEPSC frequency and spine density were decreased after cno treatment (Fig. 4d), with no change in mEPSC amplitude (direct pathway MSNs: frequency, 0.66 ± 0.2 Hz (saline) versus 0.25 ± 0.05 Hz (cno), $n = 12$ and 9; spine density, 0.60 ± 0.05 spines per µm (saline) versus 0.38 ± 0.03 spines per µm (cno), $n = 7$ and 6; indirect pathway MSNs: frequency, 0.65 ± 0.14 Hz (saline) versus 0.25 ± 0.04 Hz (cno), $n = 16$ and 16; spine density, 0.58 ± 0.03 spines per µm (saline) versus 0.31 ± 0.02 spines per µm (cno), $n = 7$ and 6) (Fig. 4d, e). Because inhibition of Rbp4-Cre^+ corticostriatal projections caused no change in locomotion at P14–15 (Supplementary Fig. 14), activity-dependent control of striatal synaptogenesis is not secondary to behavioural changes.

To determine whether activity-dependent changes in striatal synaptogenesis persist into early adulthood, we inhibited the activity of corticostriatally projecting Rbp4-Cre neurons during P8–P15 and

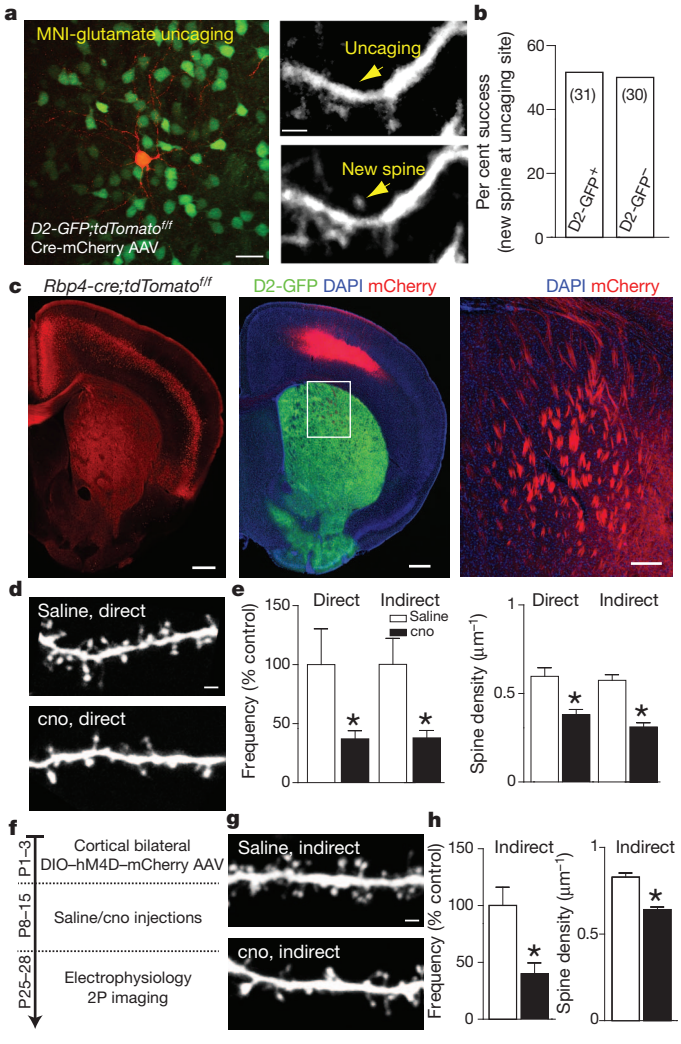

Figure 4 | Corticostriatal activity drives synaptogenesis in MSNs. **a**, Focal release of glutamate is sufficient to trigger *de novo* spinogenesis in MSNs. Two-photon laser-scanning microscopy image of tdTomato (red) and GFP (green) expressing MSNs in a *D2-GFP;tdTomato$^{f/f}$* mouse sparsely injected with Cre-mCherry encoding AAV at P0. Imaging was performed in an acute slice of striatum at P10. Scale bar: 20 µm. The right panels show a higher-magnification image of a dendrite before (top) and after (bottom) triggering new spine growth. Scale bar: 2 µm. The stimulation protocol consisted of 40 uncaging pulses directed at the indicated spot (arrow) with 15 mW of 720-nm light measured at the objective back aperture. **b**, Summary graph demonstrating ~50% success rate in generating new spines with glutamate uncaging in direct and indirect pathway MSNs at P8–11. **c**, Left: Cre expression driven by an *Rbp4* BAC (Rbp4-Cre) targets Cre to corticostriatal projection neurons. Red fluorescence from a tdTomato reporter allele is present in deep-layer cortical neurons and densely labels axons throughout striatum. Scale bar: 500 µm. Middle: AAV DIO hM4D–mCherry injected into the cortex of a mouse carrying Rbp4-Cre and D2-GFP transgenes shows strong red fluorescence in deep-layer somata in cortex and green fluorescence in striatum. Scale bar: 500 µm. Right: red channel, higher magnification view of boxed area in the centre panel shows extensive hM4D–mCherry labelling of corticostriatal axons. **d**, **e**, *In vivo* inhibition of Rbp4-Cre neurons expressing hM4D during the window of excitatory synaptogenesis leads to a decrease in excitatory synapse number for both direct and indirect pathway MSNs. **d**, Two-photon laser-scanning microscopy images of a dendrite from a direct pathway MSN in a saline-injected mouse and a less spiny dendrite from a cno-injected littermate. Scale bar: 2 µm. **e**, Summary data showing a decrease in direct and indirect pathway MSN mEPSC frequency (left) and spine density (right) for cno-treated mice versus saline-treated littermates. **f**–**h**, hM4D/cno-dependent decreases in MSN excitatory synapse number persist into early adulthood. **f**, Timeline for experiments. **g**, Two-photon laser-scanning microscopy images of dendrites from indirect pathway MSNs from sibling mice in their early adulthood (P25–28) after treatment with cno or saline during the time window for excitatory synaptogenesis (P8–15). **h**, Summary data showing that decreases in mEPSC frequency (left) and spine density (right) persist into early adulthood. Error bars indicate s.e.m.

examined excitatory innervation in indirect pathway MSNs at P25–28 (Fig. 4f). Both mEPSC frequency and spine density were reduced in cno-treated mice compared to saline-injected controls (indirect pathway MSNs: frequency, 0.73 ± 0.12 Hz (saline) versus 0.29 ± 0.07 Hz (cno), $n = 28$ and 26; spine density, 0.83 ± 0.02 spines per μm (saline) versus 0.64 ± 0.02 spines per μm (cno), $n = 10$ per group) (Fig. 4g, h). Thus, perturbations of cortex-basal ganglia–thalamus circuit activity in early life can have lasting effects into adulthood.

Our data reveal that the balance of activity in direct/indirect pathways dictates postnatal excitatory innervation of the striatum. Because manipulating striatal output alters the structure of its input, activity must act recurrently, through a polysynaptic, multi-stage circuit. The simplest explanation for these findings is that glutamate release from cortical and thalamic axons in the striatum promotes the formation or stabilization of glutamatergic synapses onto MSNs. Perturbations that result in relative activation of the direct pathway compared to the indirect (and hence activate cortex and thalamus) will drive glutamatergic synapse formation in the striatum. Collateral connections among MSNs[19] influence basal ganglia activity and may contribute to these effects. Such activity-dependent processes may be essential for refining locomotion and reward-based behaviour.

These mechanisms are fundamentally distinct from those believed to underlie topographic organization of sensory cortices during postnatal development. In these cortical areas, waves of neural activity pass information about sensory maps from one stage of processing to the next[28,29], and these mappings are translated into synaptic connectivity through spike-timing-dependent plasticity rules[30]. In contrast, striatal inputs from widespread cortical areas show only modest topographic organization. Instead of sensory maps, synaptic networks throughout the cortex-basal ganglia–thalamus loop are thought to reflect parallel, segregated loops of mixed inhibitory and excitatory projections. Here we show that activity propagates through cortex-basal ganglia–thalamus circuits to specify synaptic networks based on the balanced output of direct and indirect pathways in a manner that can, through positive feedback, select for recurrent closed loops.

METHODS SUMMARY

Viral expression in BAC transgenic mice. Injections of recombinant Cre-On or Cre-Off (A. Saunders, C. Johnson and B. Sabatini, manuscript in preparation) AAVs were targeted to striatum of D1-Cre, D2-Cre, or Adora-Cre mice. Rbp4-Cre mice were injected in the somatosensory and motor regions of the cortex. Cre-expressing AAV was injected into the striatum of conditional *Slc32a1* or *Ai14-lsl-tdTomato* mice.

Electrophysiology and two-photon imaging. Whole-cell voltage-clamp recordings were obtained from pathway-identified MSNs in acute coronal slices. Cells were filled with Alexa Fluor 594 (10–20 μM) and imaged using a two-photon laser-scanning microscope (810–840 nm).

Full Methods and any associated references are available in the online version of the paper at www.nature.com/nature.

Received 31 January; accepted 20 March 2012.
Published online 13 May 2012.

1. Wiesel, T. N. & Hubel, D. H. Single-cell responses in striate cortex of kittens deprived of vision in one eye. *J. Neurophysiol.* **26,** 1003–1017 (1963).
2. Smith, G. B., Heynen, A. J. & Bear, M. F. Bidirectional synaptic mechanisms of ocular dominance plasticity in visual cortex. *Phil. Trans. R. Soc. B* **364,** 357–367 (2009).
3. Stephenson-Jones, M., Samuelsson, E., Ericsson, J., Robertson, B. & Grillner, S. Evolutionary conservation of the basal ganglia as a common vertebrate mechanism for action selection. *Curr. Biol.* **21,** 1081–1091 (2011).
4. Yin, H. H. & Knowlton, B. J. The role of the basal ganglia in habit formation. *Nature Rev. Neurosci.* **7,** 464–476 (2006).
5. Alexander, G. E., DeLong, M. R. & Strick, P. L. Parallel organization of functionally segregated circuits linking basal ganglia and cortex. *Annu. Rev. Neurosci.* **9,** 357–381 (1986).
6. Nambu, A. Somatotopic organization of the primate basal ganglia. *Front. Neuroanat.* **5,** 26 (2011).
7. Smith, Y., Bevan, M. D., Shink, E. & Bolam, J. P. Microcircuitry of the direct and indirect pathways of the basal ganglia. *Neuroscience* **86,** 353–387 (1998).
8. Gerfen, C. R. The neostriatal mosaic: multiple levels of compartmental organization in the basal ganglia. *Annu. Rev. Neurosci.* **15,** 285–320 (1992).
9. Albin, R. L., Young, A. B. & Penney, J. B. The functional anatomy of basal ganglia disorders. *Trends Neurosci.* **12,** 366–375 (1989).
10. Kelly, R. M. & Strick, P. L. Macro-architecture of basal ganglia loops with the cerebral cortex: use of rabies virus to reveal multisynaptic circuits. *Prog. Brain Res.* **143,** 447–459 (2004).
11. Alexander, G. E. & Crutcher, M. D. Functional architecture of basal ganglia circuits: neural substrates of parallel processing. *Trends Neurosci.* **13,** 266–271 (1990).
12. Kravitz, A. V. *et al.* Regulation of parkinsonian motor behaviours by optogenetic control of basal ganglia circuitry. *Nature* **466,** 622–626 (2010).
13. Ferguson, S. M. *et al.* Transient neuronal inhibition reveals opposing roles of indirect and direct pathways in sensitization. *Nature Neurosci.* **14,** 22–24 (2011).
14. Cho, J. & West, M. O. Distributions of single neurons related to body parts in the lateral striatum of the rat. *Brain Res.* **756,** 241–246 (1997).
15. Tong, Q., Ye, C.-P., Jones, J. E., Elmquist, J. K. & Lowell, B. B. Synaptic release of GABA by AgRP neurons is required for normal regulation of energy balance. *Nature Neurosci.* **11,** 998–1000 (2008).
16. McIntire, S. L., Reimer, R. J., Schuske, K., Edwards, R. H. & Jorgensen, E. M. Identification and characterization of the vesicular GABA transporter. *Nature* **389,** 870–876 (1997).
17. Wojcik, S. M. *et al.* A shared vesicular carrier allows synaptic corelease of GABA and glycine. *Neuron* **50,** 575–587 (2006).
18. Gong, S. *et al.* A gene expression atlas of the central nervous system based on bacterial artificial chromosomes. *Nature* **425,** 917–925 (2003).
19. Taverna, S., Ilijic, E. & Surmeier, D. J. Recurrent collateral connections of striatal medium spiny neurons are disrupted in models of Parkinson's disease. *J. Neurosci.* **28,** 5504–5512 (2008).
20. Sohal, V. S., Zhang, F., Yizhar, O. & Deisseroth, K. Parvalbumin neurons and gamma rhythms enhance cortical circuit performance. *Nature* **459,** 698–702 (2009).
21. Nimchinsky, E. A., Sabatini, B. L. & Svoboda, K. Structure and function of dendritic spines. *Annu. Rev. Physiol.* **64,** 313–353 (2002).
22. Somogyi, P., Bolam, J. P. & Smith, A. D. Monosynaptic cortical input and local axon collaterals of identified striatonigral neurons. A light and electron microscopic study using the Golgi-peroxidase transport-degeneration procedure. *J. Comp. Neurol.* **195,** 567–584 (1981).
23. Tepper, J. M., Sharpe, N. A., Koós, T. Z. & Trent, F. Postnatal development of the rat neostriatum: electrophysiological, light- and electron-microscopic studies. *Dev. Neurosci.* **20,** 125–145 (1998).
24. Rogan, S. C. & Roth, B. L. Remote control of neuronal signaling. *Pharmacol. Rev.* **63,** 291–315 (2011).
25. Krashes, M. J. *et al.* Rapid, reversible activation of AgRP neurons drives feeding behavior in mice. *J. Clin. Invest.* **121,** 1424–1428 (2011).
26. Kwon, H.-B. & Sabatini, B. L. Glutamate induces *de novo* growth of functional spines in developing cortex. *Nature* **474,** 100–104 (2011).
27. Carter, A. G. & Sabatini, B. L. State-dependent calcium signaling in dendritic spines of striatal medium spiny neurons. *Neuron* **44,** 483–493 (2004).
28. Meister, M., Wong, R. O., Baylor, D. A. & Shatz, C. J. Synchronous bursts of action potentials in ganglion cells of the developing mammalian retina. *Science* **252,** 939–943 (1991).
29. Triplett, J. W. *et al.* Retinal input instructs alignment of visual topographic maps. *Cell* **139,** 175–185 (2009).
30. Bi, G. & Poo, M. Synaptic modification by correlated activity: Hebb's postulate revisited. *Annu. Rev. Neurosci.* **24,** 139–166 (2001).

Supplementary Information is linked to the online version of the paper at www.nature.com/nature.

Acknowledgements We thank Sabatini laboratory members for comments on the manuscript; B. Roth, K. Deisseroth and M. During for AAV backbones encoding hM4D, ChR2 and Cre, respectively; and C. Gerfen for the Rbp4-Cre mouse line. Confocal imaging was done through the Harvard NeuroDiscovery and Olympus Imaging Centers. This work was supported by grants from NINDS (NS046579, B.L.S); the W.F. Milton Fund Award and the Leonard and Isabelle Goldenson Research Fellowship (Y.K.); and NIH (F31 NS074842) and Shapiro predoctoral fellowship (A.S.).

Author Contributions Y.K., A.S. and B.L.S. designed the experiments. Y.K. and A.S. performed experiments and analysed data. C.A.J. assisted in experiments and genotyping. B.B.L. generated the conditional *Slc32a1* mouse. Y.K., A.S. and B.L.S. wrote the paper with contributions from C.A.J. and B.B.L.

Author Information Reprints and permissions information is available at www.nature.com/reprints. The authors declare no competing financial interests. Readers are welcome to comment on the online version of this article at www.nature.com/nature. Correspondence and requests for materials should be addressed to B.L.S. (bsabatini@hms.harvard.edu).

METHODS

Mouse strains and genotyping. Animals were handled according to protocols approved by the Harvard Standing Committee on Animal Care, in accordance with NIH guidelines. To generate mice with conditional knockout of *Slc32a1* from the direct and indirect pathway, *D1/D2-cre;Slc32a1*$^{f/+}$ mice were crossed with *Slc32a1*$^{f/f}$ mice. Conditional knockout crosses were made using either male or female parents as Cre carriers. To generate pups carrying the D1-, D2-, Adora2a- or Rbp4-Cre transgenes, D1-, D2-, Adora2a- or Rbp4-Cre parents, either male or female, were crossed to wild-type C57BL/6 mice. D2-BAC and GAD67 knock-in GFP transgenes were also introduced through either parent or both parents. A full description of the transgenic mouse lines used in this study is provided in Supplementary Table 1. Genotyping was performed from tail tissue sampled at P0.5–5. Tail tissue was digested overnight (Viagen) and PCR was performed using the lysates as template DNA. The genotyping primers are listed in Supplementary Table 2 and the PCR protocols are provided below.

PCR protocol 1: (1) 95 °C for 5 min; (2) 95 °C for 30 s; (3) 53 °C for 30 s; (4) 72 °C for 1 min; (5) repeat (2)–(4) for 35 cycles; (6) 72 °C for 5 min.

PCR protocol 2: (1) 94 °C for 3 min; (2) 94 °C for 45 s; (3) 66 °C, down −1 °C each cycle for 45 s; (4) 72 °C for 45 s; (5) repeat (2)–(4) for 9 cycles; (6) 94 °C for 30 s; (7) 58 °C for 30 s; (8) 72 °C for 30 s; (9) repeat (6)–(8) for 20 cycles; (10) 72 °C for 10 min.

Stereotaxic injections. For intracranial injections, P0–7-day-old mice were anaesthetized with isofluorane and placed into a stereotaxic apparatus. Virus was delivered at a maximum rate of 100 nl min^{-1} using a Microinject system (WPI). Dorsolateral striatum was targeted by directing the needle approximately 1 mm anterior to midpoint between ear and eye, 1.5 mm from midline and 1.8 mm ventral to brain surface, and these coordinates were adjusted based on age. Cortical injections were similarly targeted in the anterior–posterior and medial–lateral axes, but the needle was directed 0.8 mm ventral to brain surface. Unilateral injections of 350–500 nl were used to drive ChR2 expression for electrophysiology experiments, pathway tracing, cell targeting for mEPSC recordings and cell fills for dendritic spine density analyses; 500–750 nl bilateral or 50 nl unilateral injections were used in circuit manipulation with hM4D; 50 nl unilateral injections were used for sparse postnatal *Slc32a1* knockout; 50 nl unilateral injections (1:10 dilution) were used for inducing tdTomato expression in *de novo* spinogenesis experiments. Virus titres are provided in Supplementary Table 3 and injection rates were 50–100 nl min^{-1}. After injections and wound closure, mice received flunixin for analgesia and were returned to home cages for 8+ days.

Slice preparation. Coronal striatal slices were prepared as described previously for rat[27]. Mice were anaesthetized by inhalation of isoflurane. Cerebral hemispheres were removed and placed into cold choline-based artificial cerebrospinal fluid (choline-ACSF) containing 25 mM $NaHCO_3$, 1.25 mM NaH_2PO_4, 2.5 mM KCl, 7 mM $MgCl_2$, 25 mM glucose, 1 mM $CaCl_2$, 110 mM choline chloride, 11.60 mM ascorbic acid and 3.10 mM pyruvic acid, and equilibrated with 95% O_2/5% CO_2. Tissue was blocked and transferred into a slicing chamber containing choline-ACSF. Coronal striatal slices (300 μm) were then cut on a Leica VT1000 s (Leica Instruments) and transferred into a holding chamber with ACSF containing (in mM) 127 NaCl, 2.5 KCl, 25 $NaHCO_3$, 1.25 NaH_2PO_4, 2.0 $CaCl_2$, 1.0 $MgCl_2$ and 25 glucose, equilibrated with 95% O_2/5% CO_2. Slices were incubated at 34 °C for 30–45 min before recording.

Electrophysiology. Whole-cell recordings were obtained from striatal MSNs visualized under infrared differential interference contrast (IR-DIC) using patch pipettes with pipette resistance of 2.5–4.5 MΩ. To identify infected MSNs or those belonging to the indirect pathway, mCherry or GFP fluorescence was detected using epifluorescence illumination. For ChR2-evoked current recordings, a high Cl^- internal solution containing 100 mM CsCl, 35 mM CsFl, 10 mM HEPES, 4 mM $MgCl_2$, 4 mM Na_2ATP, 0.4 mM NaGTP, 10 mM Na_2CrePO_4, 1 mM EGTA (pH 7.4) was used. For miniature excitatory postsynaptic current recordings, the internal solution consisted of 120 mM $CsMeSO_4$, 15 mM CsCl, 8 mM NaCl, 10 mM TEACl, 10 mM HEPES, 2 mM QX314, 4 mM MgATP, 0.3 mM NaGTP (pH 7.4). Alexa Fluor 594 (10–20 μM) was added to internals to visualize cell morphology and to confirm cell identity as MSN. For cell-attached recordings, a caesium-based internal without Alexa Fluor 594 was used instead and traces were monitored for signs of breaking in. Recordings were made using an Axoclamp 700B amplifier (Axon Instruments) at room temperature for MSN collateral current analysis and mEPSC recordings, and at elevated temperature (34 °C) for cell-attached recordings. Data were filtered at 3 kHz and sampled at 10 kHz. Series resistance, measured with a 5 mV hyperpolarizing pulse in voltage clamp, was on average under 20 MΩ and less than 25 MΩ, uncompensated. All voltage-clamp recordings were made from cells held at −70 mV, except for a small minority of cells in which ChR2 stimulation drove unclamped spikes. In this case, cells were held at −40 mV and peak currents were multiplied by 1.75, the magnitude increase predicted by −30 mV change in driving force of Cl and confirmed by experiments where ChR2 currents were elicited at both holding potentials (−70 and −40 mV). For miniature EPSC recordings, all MSNs were held at −70 mV. Extracellular recordings were acquired in voltage-clamp mode without imposing a holding potential.

Optogenetic activation. To activate ChR2 in acute slices, 473-nm laser light (Optoengine) was focused onto the back aperture of the ×60 water immersion objective to produce whole-field illumination. To quantify the laser light delivered with each pulse, light leak through a high-pass dichroic filter was measured using a photodiode calibrated by measuring the power at the focal plane of ×60 objective. For each ChR2 activation experiment in Fig. 1, six different light intensities were used to drive postsynaptic currents (0.1–20 mW). Summary data presented in Fig. 1 are based on the strongest, 20 mW stimulation. For optogenetic activation of neurons during extracellular recording, light power was slowly increased while acquiring data until a moderate firing rate (~4–20 Hz) was achieved.

Pharmacology. Pharmacological agents were used at the following final concentrations. For ChR2-evoked current recordings, ACSF contained 10 μM CPP (Tocris Cookson), 10 μM NBQX (Tocris), 10 μM scopolamine hydrobromide (Tocris). For mEPSC recordings, ACSF contained 1 μM TTX (Sigma), 50 μM SR 95531/gabazine (Tocris), 10 μM CPP and 10 μM scopolamine hydrobromide. For extracellular recordings, ACSF contained CPP, NBQX, SR 95531 and scopolamine hydrobromide. SR 95531 was present in a subset of glutamate-uncaging-evoked spinogenesis experiments. All reagents were dissolved in distilled water and diluted to their final concentrations in ACSF on the day of the experiment, except for NBQX, which was dissolved in DMSO. Clozapine-*n*-oxide (Sigma) was used at 10 μM for slice experiments. For *in vivo* circuit activity manipulation, clozapine-*n*-oxide in sterile saline was administered subcutaneously at 1 mg kg^{-1} body weight twice daily.

Two-photon imaging. Two-photon laser-scanning microscopy was performed using a custom microscope as previously described[27]. Cell morphology was visualized using Alexa Fluor 594 (10–20 μM) excited with 810–840-nm light and introduced into the cell through whole-cell recording or single-cell electroporation. Briefly, a pipette containing Alexa Fluor 594 in dH_2O was guided to a MSN cell body with low positive pressure. Pressure was released and a single 0.2-ms-long 0.1–0.3 V pulse was delivered through an electrical stimulator (A.M.P.I) to fill the soma with dye, which rapidly diffused into dendrites and spines (~5 min). A two-photon laser-scanning microscopy three-dimensional image stack through each neuron was collected, followed by stacks through 2–3° dendritic segments at a tenfold higher magnification. For dendritic spine density and spine shape analyses, cells were coded and analysed used custom-written routines in MATLAB. Three-to-five secondary and tertiary dendrites per MSN were analysed. The size of each spine was measured in the optical section of maximal brightness.

Glutamate uncaging. Uncaging of MNI-glutamate was done on a custom-built microscope combining two-photon laser-scanning microscopy and two-photon laser photoactivation, or uncaging. Two mode-locked Ti:sapphire lasers (Coherent) tuned to 920 nm and 720 nm were used for imaging tdTomato fluorescence and uncaging MNI-glutamate, respectively. The intensity of each laser was independently controlled by Pockels cells (Conoptics). For uncaging, 2.5 mM MNI-glutamate (Sigma-Aldrich) was added to Mg-free ACSF and 15 mW of 720 nm light at the specimen was used to focally release the uncaging group. To visualize the dendrites of MSNs of known pathways, mice carrying at least one tdTomato reporter allele and a D2-GFP BAC transgene were injected with AAV carrying Cre-mCherry at P0–1. AAV injections were titred to generate sparse Cre expression in striatum. tdTomato$^+$ MSN dendrites were selected using the following two criteria: smooth dendritic membrane in the immediate location of uncaging spot and the presence of at least one dendritic spine nearby (within ~5 μm). MNI-glutamate was uncaged near the dendrite (~0.5 μm away from the edge) at 2 Hz using 40 4-ms-long pulses as described previously[27]. This protocol drives a ~7-pA uncaging-evoked EPSC in whole-cell voltage-clamp recording (Supplementary Fig. 12). Dendrite images were taken before and immediately after induction protocol.

Behavioural analysis. For measuring activity levels, 14–17-day-old mice were monitored one at a time using the large (45 × 45 cm^2) home cage module of EthoVision XT (Noldus) with centre point and nose point tracking. No food or water was provided for the 1 h duration of the recording. Comparisons were made between sibling littermates carrying 0 or 1 *Slc32a1* alleles on the same day, with genotype order counterbalanced. All recordings were done in a narrow time window in littermate mice maintained on a standard 12/12 h light/dark cycle. The distance travelled during 1 h was quantified.

AAV production. Adeno-associated virus (AAV) vector DNA was amplified in recombination-deficient bacteria (OneShot Stbl3, Invitrogen) and packaged by a commercial vector core facility (University of North Carolina). Supplementary Table 2 describes the AAV vectors used in this study. The Cre-silenced ChR2–mCherry vector (DO–ChR2–mCherry)was generated by reversing the orientation

of the ChR2–mCherry transgene with respect to the two pairs of flanking *loxP* sites using the Asc1 and Nhe1 restriction sites.

Fixed-tissue preparation, imaging and immunohistochemistry. Mice were transcardially perfused with 4% paraformaldehyde and the brains were post-fixed for 1–7 days. Brains were sectioned coronally or sagittally at 40 μm using a Vibratome. No immuno-enhancement was used to increase the signal of native fluorophores. For Cre immunofluorescence, 1:6 series of sections through the striatum were incubated overnight at 4 °C with mouse anti-Cre antibody in TBS with 0.5% Tween-20 (1:250, Invitrogen). The following day tissue was rinsed in TBS, reacted with goat anti-mouse Alexa Fluor 488 (1:500, Molecular Probes) for 1 h at room temperature, rinsed, mounted onto superfrost slides, dried and coverslipped under ProLong antifade reagent with DAPI (Molecular Probes). Images were acquired with a Zeiss LSM 510 META confocal microscope (Harvard NeuroDiscovery Center). Slides were coded for confocal microscopy and data analysis. For every animal, five fields of view were selected for analysis from several striatal sections, which matched the location of electrophysiological recordings. Two-dimensional 1-μm-thick optical sections were analysed in ImageJ using co-localization and cell counter plug-ins. The number of Cre^{+} and Cre^{-} DAPI-stained nuclei was quantified and expressed as a percentage. On average >600 cells were examined for Cre expression in every animal. The code was broken after completion of the analysis.

For parvalbumin immunofluorescence, sections were incubated in mouse anti-parvalbumin primary antibody (1:2,000, Millipore), goat anti-mouse Alexa 488 secondary antibody, and coverslipped under ProLong antifade reagent with DAPI. Image stacks were acquired with a with an Olympus FV1000 laser scanning confocal microscope (Harvard Neurobiology Imaging Facility). The number of parvalbumin-labelled, D1-Cre tdTomato reporter-positive neurons was quantified. Stacks through >300 neurons from four mice were analysed.

Whole-brain imaging. Mice were unilaterally injected with DIO–ChR2–mCherry AAV into the right dorsal striatum and transcardially perfused with 4% paraformaldehyde 8–10 days later. Brains were sectioned sagittally at 100 μm. For every brain, the slice with maximal cross-section of SNr or globus pallidus was selected for imaging with an Olympus VS110 slide scanning microscope using ×20 objective. No immuno-enhancement was needed to visualize long-range projections. For confocal imaging, sections were scanned on a confocal microscope under a ×63 oil objective. ImageJ was used to analyse fluorophore distributions and data were expressed as area fractions.

Data analysis. Offline data analysis for electrophysiology was performed using custom software written in Igor Pro (Wavemetrics) and MATLAB. Statistical analyses were done using GraphPad PRIZM 5 software (GraphPad). All values are reported as means ± s.e.m., unless noted otherwise. Statistical significance was determined by two-tailed Student's *t*-tests, with Welch's correction for data sets with significantly different variances, and two-tailed Wilcoxon signed rank test for non-parametrically distributed data. Two-way ANOVA with Bonferroni post-hoc comparisons and log-rank Mantel–Cox test were used for weight and lifespan analyses in Supplementary Fig. 3. $P < 0.05$ was considered to be statistically significant.